Surface & Coatings Technology 434 (2022) 128196

Contents lists available at ScienceDirect

Surface & Coatings Technology

journal homepage: www.elsevier.com/locate/surfcoat

Effect of geometric position on the film properties for a complex-shaped substrate in HiPIMS discharge: Experiment and simulation

Li Hua [a], Luo Yang [a], Han Mingyue [a], Tang Ling [a], Gu Jiabin [a], Li Guodong [b,c,*], Deng Dachen [a], Liu Hongtao [d], Huang Kai [e], Li Liuhe [a,**]

[a] *Department of Material Processing and Control Engineering, School of Mechanical Engineering and Automation, Beihang University, Beijing, PR China*
[b] *School of Engineering Science, University of Chinese Academy of Science, Beijing, PR China*
[c] *Institute of Mechanics, Chinese Academy of Sciences, Beijing, PR China*
[d] *Beijing Institute of Aero space Control Devices, Beijing, PR China*
[e] *Institute of Electrical Engineering, Chinese Academy of Sciences, Beijing, PR China*

A R T I C L E I N F O

Keywords:
HiPIMS
Shadowing effect
Ion dynamics
2D PIC-MCC

A B S T R A C T

The purpose of this paper is to explore the effect of geometric position on the film properties for a complex-shaped substrate in high-power impulse magnetron sputtering (HiPIMS) discharge. The substrate is a trapezoidal prism, whose base has four inner corners of 60°, 120°, 75°, and 105°. A negative bias is added to this trapezoidal prism during the high-density discharge to deposit TiAlSiN films. The chemical compositions, microstructures and mechanical properties of the films at different area of the substrate are analyzed using the energy dispersive spectroscopy, X-ray diffraction, scanning electron microscope, nano-indentor and Vickers indentation tester. Systematic investigations demonstrate that the films properties have prominent differences on various planes of the trapezoidal-prism sample, due to the so-called shadowing effect. Compared with the measurements on the plane perpendicular to the target surface, there is a higher average hardness and stronger toughness on the plane facing to the target surface. However, the values of both the hardness and toughness are the lowest on the plane facing away from the target surface. Moreover, even for the same plane, the enhanced mechanical properties as well as a smoother surface and denser microstructure appear in the edge regions, with respect to that in the planar center regions. To understand these interesting phenomena, a two-dimensional particle-in-cell/Monte Carlo collision simulation (2D PIC-MCC) and Transport of Ions in Matter method (TRIM) are employed to explore the ion dynamics at the different sites of the sample. Simulation results suggest that a higher ion flux density and larger re-sputtering rate may contribute to the improved film properties in the edge regions. These results in this paper are important for broadening the industrial applications of high ion fraction plasma sources in irregular structures, especially for cutting tools.

1. Introduction

High metal particles ionization fraction and large ion-to-metal flux ratio during film deposition are critically important for the formation of hard interstitial nitride alloys films with dense structure and improved adhesion [1–4], and thus satisfying the harsh temperature oxidation and wear resistant demand in cutting tool industry [5–7]. At present, the usual techniques with the high ionization rate of sputtered species in the physical vapor deposition are cathodic arc-related process and high-power impulse magnetron sputtering (HiPIMS) discharge, which have been widely applied on cutting tools [8–12]. The arc-related process is characterized by high ion fraction and deposition rate, but the co-deposition of macro-particles has become the main barrier to decrease abrasion [12] and provide efficient heat transfer [11] during cutting test. In contract, it is well recognized that the HiPIMS is able to prepare film with excellent adhesive strength, refined grain or nanocrystalline structure, smooth or ultra-dense surface, and excellent heat-resistance combined with hardness [13–16], which has been favored by the academia and industry.

For the HiPIMS discharge, the magnetron source is operated in a

* Correspondence to: L. Guodong, School of Engineering Science, University of Chinese Academy of Science, Beijing, PR China.
** Corresponding author.
E-mail addresses: lgd@imech.ac.cn (L. Guodong), Liliuhe@buaa.edu.cn (L. Liuhe).

https://doi.org/10.1016/j.surfcoat.2022.128196
Received 21 November 2021; Received in revised form 16 January 2022; Accepted 31 January 2022
Available online 5 February 2022

pulsed mode with a high pulse voltage up to kV or large instantaneous power density of kW*cm^{-2} in a short pulse duration (typically few hundred microseconds) with a low duty (less than 5%) [17–20]. Such a higher input allows the plasma density in front of the substrate to reach an order of 10^{17}– 10^{18} m^{-3} [17,20–23] and the ionization fraction of sputtered target particles to be >90% [21]. In this case, *via* a negative bias, it is possible to control the ions bombardment energy, affecting their phase compositions, microstructures, morphologies as well as mechanical properties. For examples, Xu et al. [24] observed that at a bias voltage of −150 V, the (AlCrTiVZr)N high-entropy alloy nitride films synthesized by HiPIMS presented a compact and featureless structure with preferred orientation of (111) and a small grain size of 11.3 nm, which made the films with a super hardness of 48.3 GPa. As reported by Lin et al. [25], with the magnitude of the bias voltage, the crystalline size of VO_2 thin film reduced significantly, and the temperature of phase transferring from a monoclinic to a rutile structure decreased as well. These properties for the HiPIMS-prepared films above-mentioned were measured on the planar substrates. Furthermore, for the non-planar regions of a complex-shaped geometry, applied alone or in combination with auxiliary methods, a negative bias makes the selective or uniform depositions of growth films available. For instances, for the trenches structure, Alami et al. [2] and Balzer and Fenker et al. [17] have successfully used a negative bias in HiPIMS to deposit the films on the sidewalls with smooth and dense structures, and thus enhancing the films mechanical properties. With a substrate bias and a rotation system for the complex-shaped samples, the relatively uniform films around the cutting edges [26] and the gear wheel cogs [27] were also realized in HiPIMS. Recently, even an auxiliary magnetic field is added to the biased substrate, an improved conformal coverage on the micro-trench is obtained. However, the shape effect of a biased substrate on the HiPIMS-deposited films is still ambiguous, which can influence the impinging dynamics of ions, such as ion flux density and incident angle, and thus affect the film properties of work pieces, the cutting tool for instance.

In the early days, during the investigation of plasma response in an immersed wedge-shaped cathode, Donnelly and Watterson et al. [28,29] have found that the electric field line was concentrated toward the wedge tip and larger with respect to that around planar region. As a result, the trajectories of ions became focusing toward the edge, and the incident angles of ions vary from perpendicular to of the surface (in the planar region of the wedge) to along the wedge plane of symmetry (in the edge region), both of which may result in sputtering around the edge regions. It is expected that the film properties are different between edge regions and planar regions. Considered the un-uniform ion distribution in HiPIMS deposition system [30,31], these differences in film properties may be reduced in some extent with a substrate rotation system or other auxiliary methods, yet they are inevitable. Moreover, to our knowledge, for many coated special-shaped cutting tools, the film properties are always measured on planar samples, while what limits their life are often the film properties around edges. Although *via* these film measurement methods, coated special-shaped cutting tools with superb performances still could be found, the film properties in edge region and the differences between edge region and planar surface of cutting tools are rarely reported in HiPIMS discharge to our knowledge.

In view of analysis mentioned above, we investigate the film properties in the edge region and the differences between edge region and center region for a biased trapezoidal prism in a HIPIMS system. In order to provide an effective instructional guidance for the cutting tools, the typical angles for cutting tools are designed on this trapezoidal-prism substrate. The spatially-resolved and edge-related film properties of the planes are studied on the trapezoidal-prism substrate, coated with TiAlSiN films (common investigated in industrial applications), experimentally by methods of characterization. And in the final section of our work, we analyze the ion dynamics theoretically *via* 2D Particle-in-cell/Monte Carlo collision (PIC-MCC) simulation, and study the dependence of the film properties for a complex-shaped substrate on the ion flux and re-sputtering rate in HiPIMS discharge.

2. Methodology

2.1. Film deposition

To reduce the gas breakdown delay during the glow discharge in HiPIMS, a direct current (dc) power was applied on the target during the pulse off-time (home-made supply), generally called as the pre-ionized HiPIMS. The high-speed steel was chosen as the substrate, which is intentionally machined as a trapezoidal prism, whose base has four inner corners of 60°, 120°, 75°, and 105°, as shown in Fig. 1(b). In this geometry, considering the inclination angle of planes with respect to target surface, the plane facing the target surface (the inclination angle equals to 0°) is defined as the *f*-plane, the plane facing away from the target surface (the inclination angle equals to 180°) is defined as the *b*-plane, and the plane perpendicular to the target surface (the inclination angle equals to 90°) is named as the *p*-plane, respectively.

The sintered $Ti_{0.46}Al_{0.45}Si_{0.09}$ mosaic target, made by mosaicking rectangular Ti chips into a $Ti_{0.4}Al_{0.5}Si_{0.1}$ plate, was vertically mounted in front of the magnets and cooled by the recycling water. The work surface of the target is with an ellipse area of ~95 cm^2 (12 cm in major axis × 10 cm in minor axis). The unbalanced magnetic field (Type II) was configured where the maximum strength parallel to the target surface was ~50 mT. The detailed description about the target configuration can be found in our previous works [32,33].

Prior to the film deposition, the substrate was mechanically polished and ultrasonically cleaned in ethanol, and the vacuum chamber was pumped to a base pressure of 2.0×10^{-3} Pa. The substrate was etched by glow discharge for 30 mins at pressure of 1.5 Pa in argon gas and a bias dc voltage of −800 V to remove surface contaminants and oxidations. During the TiAlSiN film growth, the working gas pressure was maintained at 0.8 Pa and the gas mixture consisted of argon (Ar, 99.999% in purity) and nitrogen (N_2, 99.999% in purity) gases, where Ar and N_2 serve as the working gas and reactive gas respectively. The schematic diagram of our deposition apparatus is shown in Fig. 1(a). The distance between the cathode target and substrate was a constant of 80 mm. The dc component during the HiPIMS is 0.1 kW. The HiPIMS was operated at a −900 V target negative voltage, a 200 μs pulse duration, and the 50 Hz repetition frequency, as shown in Fig. 2. And the substrate is added a bias voltage of −200 V. No sample rotation was employed, for that our substrate is a complex geometry, considering the distance and ion incident angle between the edges or corners and target, the rotation system even with a variable speed may not significantly reduce the shadow effect, but even will increase the cost. The detailed deposition parameters and the thickness of TiAlSiN films on the substrate are listed in Table 1. Moreover, to confirm authenticity of collected mechanical data, we deposited five samples at least under the same deposition parameter.

2.2. Characterization

The target voltage was monitored by a 100 times attenuation probe (Agilent 10076B), and the target current was measured *via* a Hall sensor (CWT Rogowski Current Transducer). Both the target voltage and current waveforms were recorded by a digital oscilloscope (Agilent Technologies DSO-X 2024A) at 128-pulse average acquisition mode. The chemical compositions, surface and cross-sectional morphology, and thickness of the TiAlSiN films were analyzed by the energy dispersive spectroscopy and scanning electron microscope (SEM-ZEISS-Gemini SEM 500, Oberkochen, Germany). The crystal and texture structure were identified by the X-ray diffraction (XRD: D/Max 2500) with CuKα radiation. θ–2θ scans were conducted in the 2θ range from 20° to 90°. The hardness and modulus of the films were obtained using nano-indentation tester (Nano-Indentor G200, Agilent) with a load precision of 50 nN in a continuous stiffness mode (CSM). The indentation depth

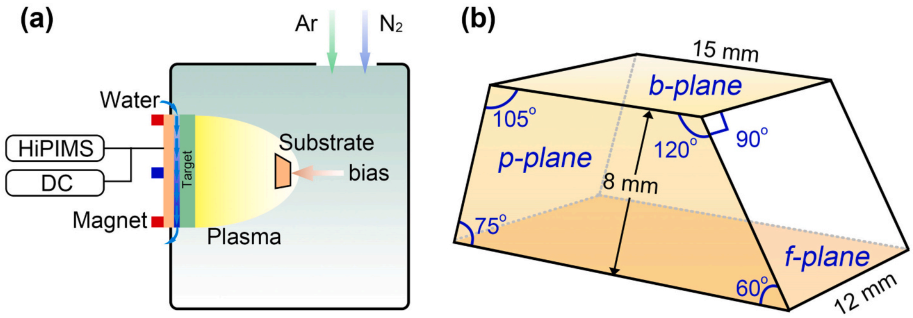

Fig. 1. The schematic diagram of (a) the experimental deposition system; (b) the geometric shape of the trapezoidal-prism substrate.

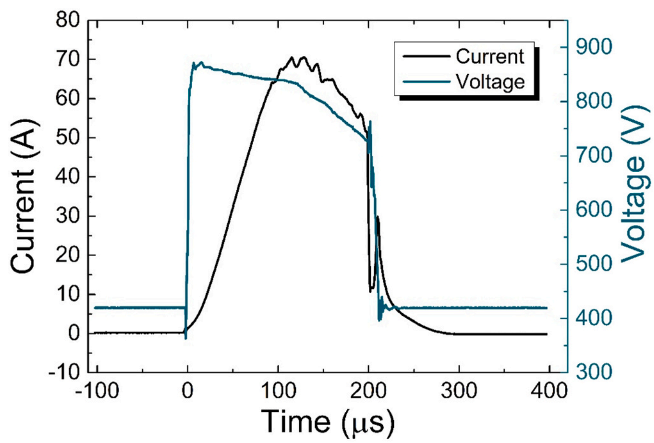

Fig. 2. The voltage and current waveform of the $Ti_{0.46}Al_{0.45}Si_{0.09}$ target.

Table 1
Deposition parameters of TiAlSiN films and film thickness.

Parameters	Values
Base pressure (Pa)	2.0×10^{-3}
Deposition pressure (Pa)	1.0
The ratio of gas N2 and Ar	1:3
dc average power (kW)	0.1
Negative pulse voltage (V)	−900
Negative pulse duration (μs)	200
Peak current during pulse duration (A)	68
Substrate biased voltage (V)	−200
Film thickness on *b*-plane (μm)	0.53–0.6
Film thickness on *p*-plane (μm)	0.85–1.0
Film thickness on *f*-plane (μm)	1.85–2.26

did not exceed 1/10 of the film thickness. The film toughness was evaluated by the H^3/E^{*2} ratio calculated from the nanoindentation measurements, where H is the hardness measured by the nano-indentation tester, and E* (=E/(1-υ^2), E represents the Young's modulus, and υ represents the Poisson ratio (~0.25)) is the effective modulus of the film. Then a micro-Vickers tester (Vickers-Indentor, Wolpert-401MVD, Chicago, IL, USA) with an applied load of 100 g was used to further investigate the indentation toughness of the films. For the hardness measurements, considering the symmetry of our substrate, we selected typical ten regions with features on the same plane, as shown schematically on *f*-plane in Fig. 3. In the center region (marked as ①), the measured intervals were set regularly at ~200 μm. The starting point of this center region is around the plane center, and the direction is pointing sideways. For other nine regions (marked as ②-⑩), the hardness values were measured along the arrow direction accordingly, with the measured step interval of (i) 50–100 μm within the measurement distance of <300 μm from the sampling starting points, (ii) 100–200 μm in the measurement region of 300–800 μm, and (iii) variable value in the measurement region of >800 μm where the interval step would be increased if the difference among the first five test points was not obvious, or 100–200 μm would be used until meeting the measurement points from the center region.

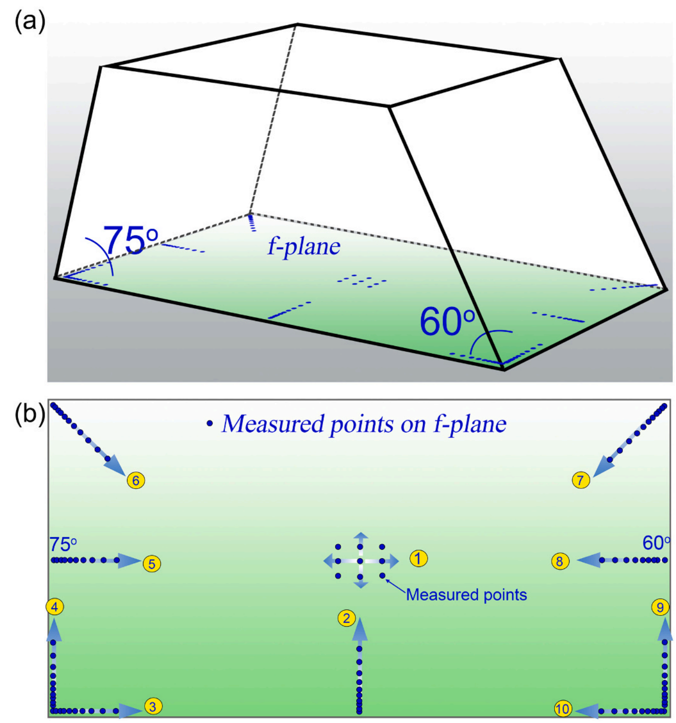

Fig. 3. Schematic diagram of measurements on the film hardness value (example of film on the *f*-plane).

2.3. PIC-MCC numerical simulation

Since firstly developed in 1980s by Hockney and Eastwood [34], PIC numerical simulation has been quickly adopted as a useful tool to simulate electrical plasma by Liberman, and Allan [35]. The simulated results from it have also been confirmed by experiments, such as the discharge voltage and current waveform, a transitory double layer at the beginning of the discharge pulse, electrons dynamics and the position of the implant fluences [36–38]. Recently this methodology has also been used in our group to study the plasma behaviors in HiPIMS discharge and BP-HIPMS discharge respectively [39,40] and the simulated results were well consistent with experimental ones, such as the enhanced plasma flux with coil magnetic field, the plasma dynamics during the gas breakdown phase and so on. Herein, we will use the 2D PIC-MCC to analysis the plasma dynamics around the trapezoidal-prism substrate.

In the 2D PIC-MCC, we defined a coordinate system: *r*-*z* plane, where the origin is the target center, *r* represents the radial direction parallel to the target surface and *z* is the axial direction perpendicular to the target. It was executed for the typical cylindrical sputtering target structure where both the magnetic field and the electric field are axisymmetric. This simulation is developed on the basis of our previous works as described in [36,41,42]. Herein we introduce it briefly.

In this simulation, the model was shown schematically in Fig. 4(a). Under the premise of the accurate and stable operation of the program, we arranged the simulated scale as close as possible to the experimental set-up, such as, 100 mm in diameter of the cathode target, 2 mm in distance between the target and anode, and 60 mm in distance between the target and substrate (where the electric field features around the substrate are almost similar to our experimental 80 mm substrate-target distance). During the simulation, the temperature, working pressure, cathode target voltage, and substrate bias were appointed at 300 K, 0.8 Pa, −800 V and −200 V respectively. The anode and vacuum chamber were grounded.

The 2D vector map of magnetic field is also presented in Fig. 4(b). The maximum radial component of magnetic field B_R was also ~50 mT parallel to the target surface. Considering the calculation time, the so-called super particles were set to represent 2×10^7 real particles [37]. Three kinds of collision events were considered and treated as Monte Carlo collision, those were (i) ionization $Ar + e \rightarrow Ar^+ + 2e$, (ii) excitation $Ar + e \rightarrow Ar^m + e$, and (iii) elastic scattering $Ar + e \rightarrow Ar + e$. The threshold energies of ionization and excitation of Ar atom were set at 15.76 eV and 11.5 eV respectively, according to the data from National Institute of Standards and Technology (NIST) [43]. The reaction cross sections for Ar in this calculation are extracted from [44]. And a random number generated between 0 and 1 was used to estimate the collision types incorporated with a null collision method [45].

To ensure the convergence, accuracy and time-saving of our numerical calculation, the cell size $dr \times dz$, total number of nodes, time step, and the inner corners of substrate mode were set at 1×1 mm^2, 123,101, 5.4×10^{-11} s, and 45°and 63.4°, respectively. For the 63.4°corner design, it is to explain the ion dynamics around the 60° corner of our substrate, and the 45° corner design is to give some guidance to substrate geometry design for film deposition. Moreover, Ar^+ ions were inserted in the simulation loop according to the target etching curve to make sure the calculation closer to the sputtering process. The rationality that Ar+ ions instead of metal ions were inserted based on two points. First one, only the relative intensity of the simulated ion flux and re-sputtering rate were used to explain the bombardment effect, which is almost free from ion species, considered the fact that the ion density as mentioned below is consistent with the metal ion density in normal HiPIMS discharge. The other one is that using Ar+ instead of metal ions to analyze the plasma parameters has been widely reported to be effective in other papers [37], as well as the references shown by our group [39,40,41]. The initial density of charged particles, $t = 0$ μs, was given 2×10^{14} m^{-3}. When the numerical calculation reached $t = 1.62$ μs, which took more than 3 weeks to calculate this time span, the plasma density reaches to 1.7×10^{17} m^{-3} during our simulation, which was consistent with normal HiPIMS discharge. Furthermore, here the PIC simulation is used to explore the ion dynamics differences between the edge region and the center region for the same plane on the substrate, not for absolute value. Thus, the ion motions at this moment are used to analyzed the film properties distribution during this present work.

3. Results and discussion

3.1. Film hardness distributions and toughness

The hardness distribution on various planes is presented in Fig. 5. It can be noticed that the hardness value appears a big difference not only among various planes abut also on different positions of the same plane. In detail, compared with the measurements on the *p*-plane, there is a higher average hardness on the *f*-plane, whereas the value of the average

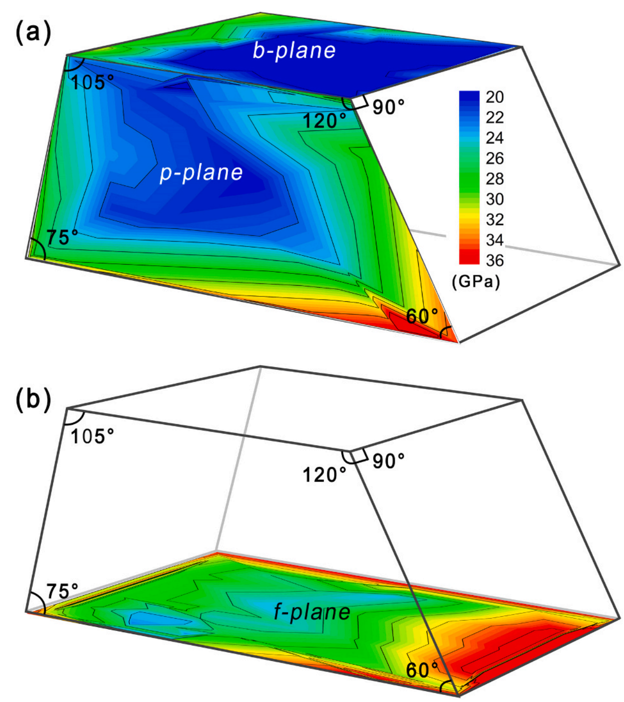

Fig. 5. Hardness distribution of TiAlSiN films dependence on the *f*-plane, *b*-plane, and *p*-plane of the trapezoidal-prism substrate.

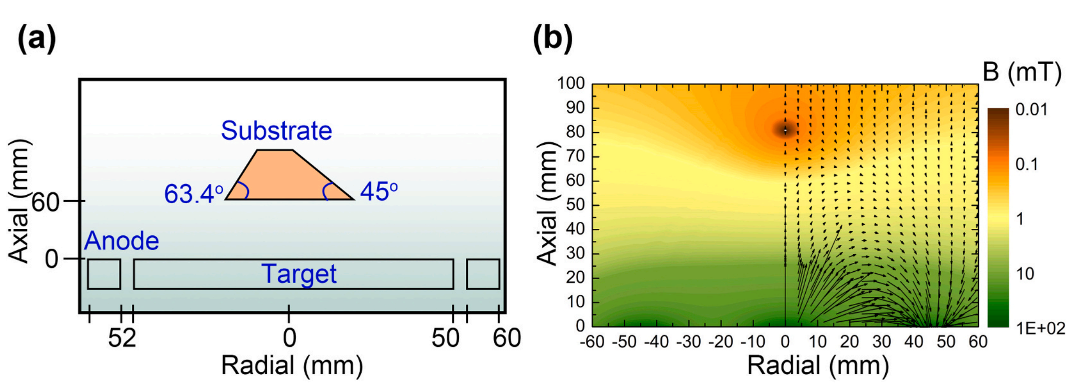

Fig. 4. Schematic plot of (a) the 2D PIC-MCC model; (b) the magnetic field distribution simulated by finite element (the righthand color map corresponds to the magnetic field strength and the arrow is the magnetic field vector).

hardness on the *b*-plane is the lowest among these three planes. For all the plane, the maximum hardness values always appear at the corner or in the edge regions of the corner, and the minimum hardness values in the center regions. Concretely, for the *f*-plane, the highest hardness region appears in the edge region of the 60° corner, with the value of 36 GPa–42 GPa, while the lowest hardness region is in the center region, with the value of 24 GPa–26 GPa. The *p*-plane shows the appearance of highest hardness region at the 60°corner, with the value of 31 GPa–37 GPa, and the lowest hardness region in the center region, with the value of 20 GPa–24 GPa. For the *b*-plane, the edge region of the 105° corner is the highest hardness region, with the value of 27 GPa–31 GPa, and its center region is the lowest hardness region, with the value of 15 GPa–23 GPa. Moreover, as the corner angle increases, the affected edge region becomes narrower and its average value is decreased, as the comparison between the affected edge region of 60° corner and that of 75° corner for the *f*-plane (marked with green color in Fig. 5), or even the affected edge region disappears for the *b*-plane at120° corner.

The film toughness has also been quantitatively estimated by the H^3/E^{*2} ratio as reported in [46,47]. Herein, the mechanical properties of TiAlSiN films listed in Tab. 2 are extracted from the corner or in the edge regions of corner (highest hardness region) and center regions (lowest hardness region) for the *f*-plane, *p*-plane, and *b*-plane respectively. In this table, we can clearly note that the regions of TiAlSiN films with the highest hardness on the *f*-plane, *p*-plane, and *b*-plane have an average H^3/E^{*2} ratio of ~0.414, 0.342, and 0.271 respectively, while those with the minimum hardness on the *f*-plane, *p*-plane, and *b*-plane merely have an average H^3/E^{*2} ratio of ~0.205, 0.146 and 0.119. The average H^3/E^{*2} ratio of films on the *f*-plane, *p*-plane, and *b*-plane are ~0.3095, 0.244, 0.195, which means that the film on the *f*-plane present strongest toughness among these three planes. Moreover, those high hardness values and large H^3/E^{*2} ratios of the film in the edge region of the smaller corner angles or in the smaller corner of the same plane give us a straightforward sign that the growth films in these regions are with hard yet tough features.

To further investigate the toughness differences of the film between the edge region and center region of the same plane, the Vickers indentation method was applied in the edge region of 60° corner and center region for the *f*-plane, as shown in Fig. 6. It can be seen that the TiAlSiN film in the center region exhibits obvious cracks, which is attribute to its low toughness. Whereas the film in the edge region displays some edge cracks (arrow) just outside the contact area of the indentation, absence of radical cracks. These results here indicate that the TiAlSiN film in the edge region indeed exhibits better toughness than that in center region, which is consistent with the results from the H^3/E^{*2} ratio measurements as analyzed in the last paragraph.

3.2. Chemical composition and microstructure

In a general way, the chemical and microstructural composition of film and the shape of substrate are always thought as the factors affecting the film hardness and toughness [47,48]. In this section, we will first explore the microstructure and chemical composition of TiAlSiN films on the three studied planes and then explore those on the same plane to uncover the incomprehensible mechanism of these various

Table 2
The mechanical properties of TiAlSiN films at the corner or in the edge regions of the corner (highest hardness region) and center regions (lowest hardness region) for the *f*-plane, *p*-plane, and *b*-plane.

Region of film	H (GPa)	E* (GPa)	H^3/E^{*2}
f-plane-center region	24.8 ± 1.0	273.1 ± 12.0	0.205
f-plane-edge region	39.3 ± 2.4	382.9 ± 30.0	0.414
p-plane-center region	21.5 ± 1.6	260.5 ± 17.7	0.146
p-plane-edge region	35.4 ± 2.6	360 ± 36.1	0.342
b-plane-center region	19.4 ± 3.2	247.3 ± 22.3	0.119
b-plane-edge region	29.0 ± 1.4	300.0 ± 23.9	0.271

hardness distributions.

Dependent on the hardness value distribution for the same plane, we select different numbers of EDS tested regions, and then take the average of all atomic ratios to be the film chemical composition for this plane. Moreover, the number of selected points in each region was almost linearly proportional to its area, to eliminate some systematic bias and reflect the actual average composition of films. For example, as for the film on the *f*-plane, based on the hardness value distribution as shown in Fig. 5(b), ten ranges were chosen in the highest hardness region, five ranges were selected in the center regions with 24 GPa–26 GPa hardness value, and ten ranges were randomly picked out in the region between highest hardness and lowest region. In the edge region with higher hardness value of 75° corner, we also take ten ranges at random. This averaging procedure was also applied on the other two planes. The average atomic ratios and the standard deviations of Ti, Al, N on the *f*-plane and the *b*-plane have been normalized to 100% and presented in Tab. 3, indicated by the fraction of $C_{Ti} = Ti/(Al + Ti + Si)$, $C_{Al} = Al/(Al + Ti + Si)$, and $C_N = N/(Al + Ti + Si)$ [33]. The compositions of films on the *b*-plane, *p*-plane and *f*-plane all present close to stoichiometric $(Ti,Al,Si)N_y$ ($y \approx 1$). Whereas film on *f*-plane shows obviously titanium content higher than aluminum content. Considering the inclination angle of planes with respect to target surface, the shadowing effect is introduced, which has already noticed in magnetron sputtering [49]. This shadowing effect can affect the energy and the number of incoming ions to substrate surface. For the *f*-plane, compared with the other two planes, there is no geometrical shielding effect, while for the *b*-plane, the shadowing effect is significant. Eventually, it seems that the flux from ion bombardment toward the *f*-plane is strongest among the three studied planes, then that toward *p*-plane is followed, and the weakest ion flux appears on the *b*-plane. In addition, light Al atoms are easier re-sputtered than heavier Ti atoms by bombarded ions with high energy. As a result, the Al depletion is more serious for the film on the *f*-plane than on the *p*-plane. The higher Al concentration for the film on the *b*-plane may be the result from the weakest re-sputtering effect and the higher sputtering yield of Al in our target compared with Ti.

The X-ray diffractograms of TiAlSiN films on the three planes are shown in Fig. 7. The diffraction peaks of the standard face-centered cubic TiN (*c*-TiN, #JCPDF38-1420) and cubic AlN (*c*-AlN, # JCPDF25-1495), and the peak of high-speed steel substrate (c-Fe3W3C, # JCPDF41-1351) have been noticed and tagged. All films exhibit an fcc-structure. No visible silicon related phases can be found, suggesting that Si atoms have probably been incorporated in the FCC lattices or formed amorphous SiNx [50–52]. The Al-rich film on the *b*-plane $((Ti_{0.44}Al_{0.48}Si_{0.08})N_{0.89})$ shows stronger (200) and (220) peaks correspond to *c*-AlN. While with the Ti content increase on the *p*-plane, the (200) and (220) peaks of *c*-AlN become weaker, and for the Ti-rich film on *f*-plane $((Ti_{0.51}Al_{0.44}Si_{0.05})N_{0.87})$, the XRD peak positions are closer to the diffraction peaks of *c*-TiN, and (220) peak of *c*-AlN disappears. Thus, it suggests that apart from *c*-AlN structure, some Al atom may exist as solid solution in the *c*-TiN crystal for the films on these three studied planes, which is consistent with the diffraction peaks at 2θ–75° between the (311) peaks of the standard *c*-TiN and *c*-AlN, and contributes to the average hardness value differences among these three studied planes are expected. Moreover, the peak positions of the film can also be influenced by the residual stress. Then the change of the preferred orientation and the minor angle offset will be analyzed in view of the residual stress. Considering the effects of the film surface roughness and thickness on the intensity of XRD patterns, we will use the relative intensity to analyze the crystal orientation and angle offset.

In general, the preferred orientation in the film is the outcome of the lowest overall energy resulting from the critical competition of the strain energy, surface energy, and stopping energy of various lattice planes [48]. The growth film on the *b*-plane is bombarded by the lowest energy flux due to the shadowing effect, and thus has a thickness of a bit more than 0.5 μm. The strain energy of this thickness range will favor the orientations of dense packed structure, (111) and (220) in cubic NaCl-

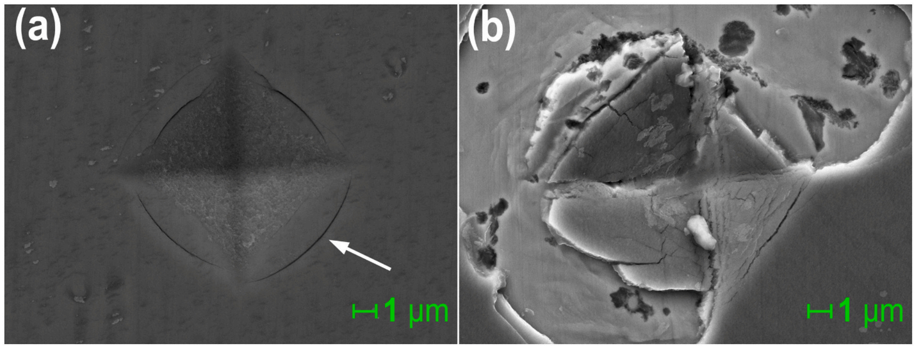

Fig. 6. The surface morphology of the indentation generated by Vickers indenter of the TiAlSiN film in the edge region of 60° corner (a) and center region (b) for the *f*-plane.

Table 3
Average chemical composition of films on the *f*-plane, *p*-plane, and *b*-plane.

Plane	C_{Ti}	C_{Al}	C_N
b-plane	0.44 ± 0.03	0.48 ± 0.02	0.89 ± 0.01
p-plane	0.45 ± 0.01	0.46 ± 0.01	0.88 ± 0.01
f-plane	0.51 ± 0.01	0.44 ± 0.01	0.87 ± 0.02

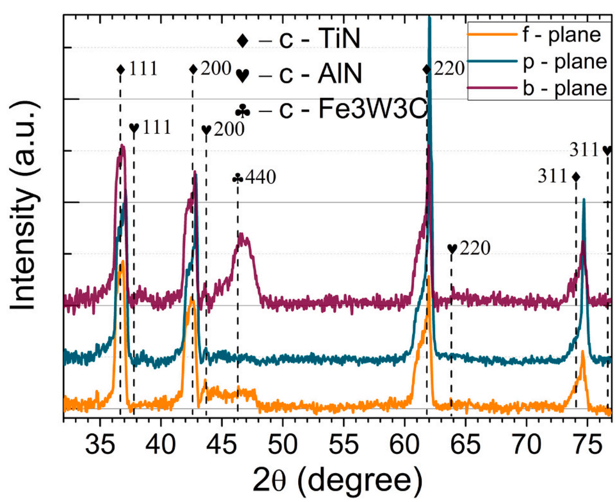

Fig. 7. The X-ray diffractograms of TiAlSiN films *versus* the *f*-plane, *p*-plane, and *b*-plane.

structure as report by Pelleg et al. [53]. As comparison with that toward the film on *b*-plane, the ion bombardment toward the film on *p*-plane (~0.85 μm-thick) is higher as stated in the chemical composition part, and significantly prefers the orientations of (220) plane, which is in line with ParK et al. [54] and Molarius et al. [55] reports. The slight rightward shift of XRD pattern of the film on *p*-plane may be attributed to stress relaxation caused by the thermal effect associated with the ion bombardment. As for the XRD patterns of film on *f*-plane, considering that some compressive strain caused by the film thickness (~2 μm) and ion bombardment was relaxed *via* heat accumulation brought by the ion bombardment [56], XRD peaks for the film on the *f*-plane shows little increase in the relative intensity I_{111}/I_{200} and small leftward shift in comparation with those for the film on the *b*-plane.

In view of analysis mentioned above, the intensity of ion bombardment has a significant impact on the chemical composition, phase composition and the stress state. Compared with that on the *b*-plane, the intensity of ion bombardment is stronger on the *p*-plane and favors the preferred orientation of (220) plane in the ceramic cubic phase, which contributes to higher average hardness of growth film. Meanwhile, the strongest intensity of ion bombardment on the *f*-plane results in the growth film with the characteristics of dense packed planes orientation, ceramic cubic phase with high Ti content, and compressive stress, which contribute to the highest average hardness and strongest toughness of the film (as shown in Fig. 4 and Table 2).

The mechanism of the hardness distribution for the same plane will be analyzed in the forthcoming paragraphs. Herein, according to the fact that the map of hardness distribution for the same plane is almost similar among these three planes as reported in Section 3.1, only the hardness distribution on the *f*-plane is analyzed as typical.

To investigate the edge-related high-hardness and strong-toughness, Fig. 8 and Table 4 display the microstructural and chemical composition of the films in the edge region and center region for the *f*-plane. From Fig. 8, we can note that the TiAlSiN film in the center region, as shown in Fig. 8(d) (f), is rougher than that in the edge region of 60° corner shown in Fig. 8(c) (e). At the same time, we can notice that the rough surface morphology is full of ripples, while the smooth surface appears compaction. Thus, the film in the edge region is smoother and denser in the edge region of 60° corner, with respect to that in the center region. But its thickness is much thinner. The absence of film at the edge (Fig. 8 (a)) may have been caused during the process of cross-section structure by hand. Moreover, as shown in Table 4, the film in the edge region of 60° corner shows obvious higher Ti and lower Al content. As the corner angle increased to 75°, the atomic ratio of Ti to Al decreased yet still larger than that of center region. The element content of the film in the center region is aluminum-rich. It seems that the higher Ti content and denser structure in TiAlSiN film are the main reasons for the high hardness value near the edge region of corner for the same plane.

3.3. The interactions between ions and edge regions

In this section, we will study the shape effect of a biased substrate on the film hardness and toughness. As stated in the introduction, the shape of a biased substrate can affect the ion flux density and incident angle of ions, and in return determine the film properties. Therefore, we will explore these ion behaviors around a negatively biased structure through a two-dimensional Particle-in-cell/Monte Carlo collision simulation (2D PIC-MCC) and the Transport of Ions in Matter code (TRIM) in this section. First, we display the potential distribution around the substrate and show how it controls the ion trajectories in front of the *f*-plane. Then, we show ion flux density distribution and calculate the re-sputtering rate. Finally, the correlations between edge-related film properties and ion dynamics are uncovered.

From Fig. 9(a), we can see that the magnitude and spatial distribution of potential strongly depend on the substrate shape. The potential line is visibly contracted near the shaper edges, which is consistent with the report in [28,29,57,58]. The highest degree of contraction occurs in the region around the edges of 45° corner which means that the electric field intensity is the strongest. In the meanwhile, the potential lines are

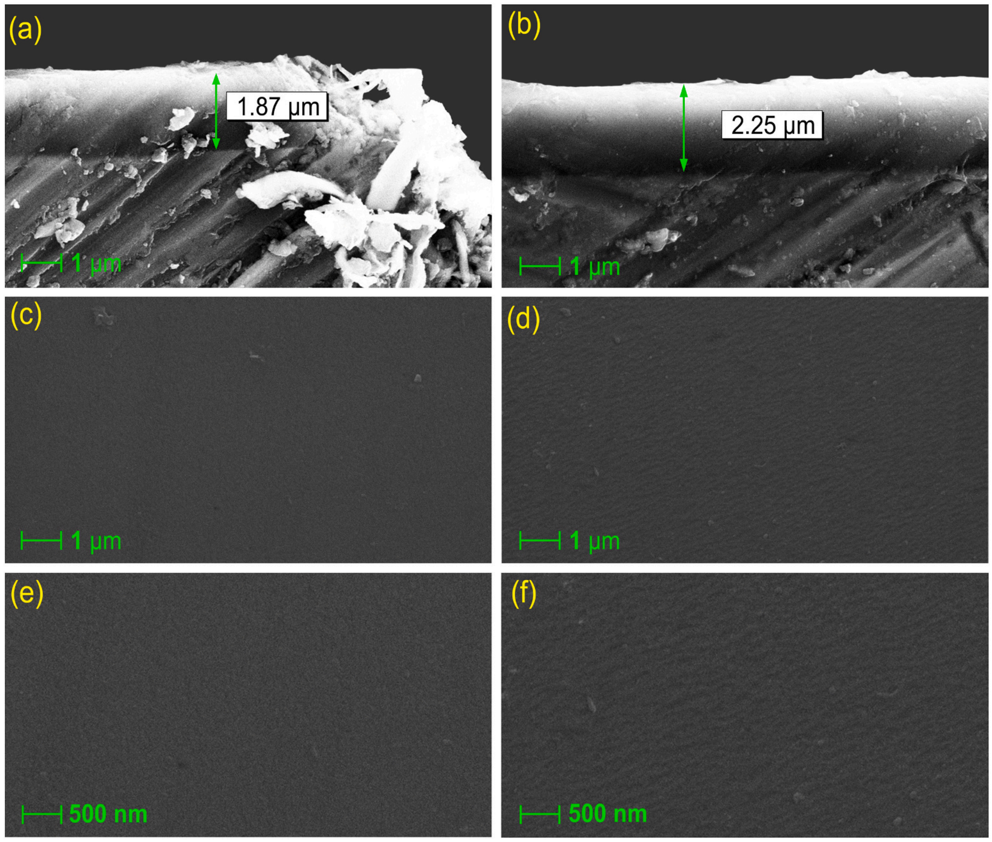

Fig. 8. The surface and cross-sectional morphologies of TiAlSiN film in the edge region of 60° corner (a) (c) (e) and center region (b) (d) (f) for the *f*-plane. (e) and (f) are enlarged image in (c) and (d) respectively.

Table 4
The atomic ratio of TiAlSiN film *versus* the different positions for the *f*-plane.

Position on the *f*-plane	C_{Ti}	C_{Al}	C_N
Edge region of 60° corner	0.57 ± 0.01	0.38 ± 0.01	0.85 ± 0.01
center region	0.43 ± 0.01	0.48 ± 0.01	0.90 ± 0.01
Edge region of 75° corner	0.53 ± 0.01	0.43 ± 0.01	0.85 ± 0.01

much divergent or incompact in front of the center regions of each edge where the intensity of electric filed is much weaker. One may notice that the distance from the substrate to the target is 60 mm, which seems inconsistent with our experimental set-value. In fact, these potential features at $z = 60$ mm are nearly similar with the 80 mm substrate-target distance, moreover, the forthcoming analyses of ion dynamics are conducted with respect to the planar center regions. Therefore, this set distance during simulation can be acceptable.

The ion trajectories are affected by electric field in a way as shown in Fig. 9(b). The ion varies continuously from perpendicular to the edge center to oblique toward the edges. Here, the ion perpendicular to the surface is at an angle defined as 0°. For the edge region of the 45° corner, the incident angle of the ion changes from 0° to ~58°, while it changes from 0° to ~50° for the 63.5° corner.

The incident angle of ions will have a significant impact on the sputtering yield of deposited particles in the edge region (re-sputtering effect). We use a free TRIM code [59] to roughly figure out their relationship, where a layer of $Ti_{0.46}Al_{0.45}Si_{0.09}N$ is bombarded by Ar^+ ions with the energy of 200 eV, as displayed in Fig. 10. The sputtering yield is enhanced with the increase of the incident angle, then reaches the maximum at ~75° for the light elements (Al, Si, N) and ~70° for the heavy element Ti, which are followed by a decrease till to 89.9°. From this figure, we can obtain that, for the film on the *f*-plane, the maximum

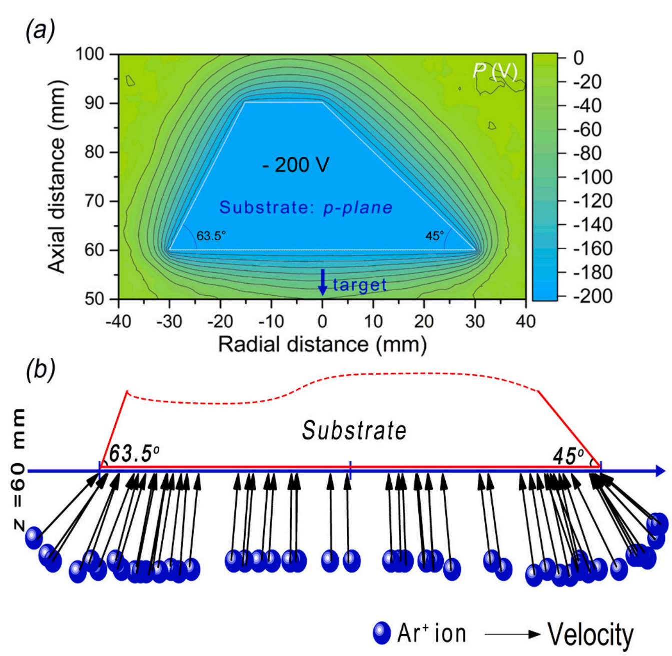

Fig. 9. (a) 2D maps of the potential around the substrate (*r*-*z* plane) and (b) the incident angle of the bombarding ions calculated by the PIC-MCC simulation at $z = 60$ mm.

sputtering yield is ~3 in the edge region of the 45° corner, and ~2.5 for the edge region of the 63.5° corner, with respect to that in the center region.

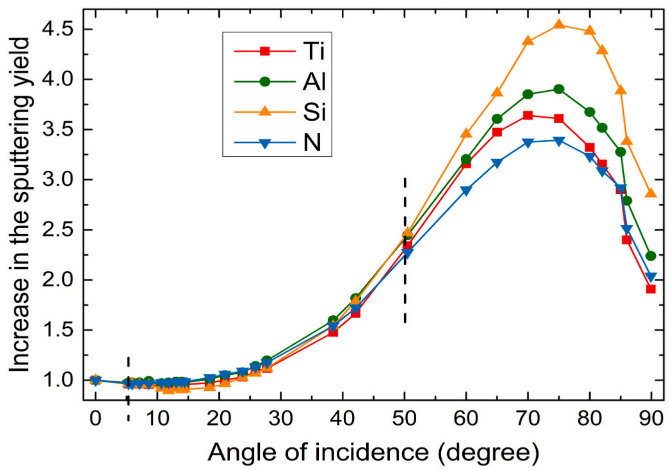

Fig. 10. The sputtering yield of different element dependence on the incident angle of the ions calculated by TRIM simulation. The sputtering yield shown is relative to that at 0° incident angle. The composition of the bombarded TiAlSiN layer is set at Ti:Al:Si:N = 0.46:0.45:0.09:1, and the incident Ar^+ ions are with energy of 200 eV.

The rise of incident ion number per unit area can also increase the re-sputtering rate. Then, ion flux density in front of *f*-plane at *z* = 60 mm relative to that in the center region is also sketched out and displayed in Fig. 11. Constrained to our designed cell size 1 × 1 mm^2, the points of ion flux density along radial distance fluctuates significantly. But we still can clearly note the trend that ion flux of ion bombardment is stronger in the edge regions than in the center region for the *f*-plane. Moreover, the flux at *r* = 29 mm (the edge of 45° corner) is ~4.5-fold of that at *r* = 0 mm (center region). Then the re-sputtering rate [58] at the edge of 45° corner can be up to 13.5 higher than that at r = 0 mm, which may result into regions without film.

The 63.5° corner designed in the simulation is closer to the 60° corner in our substrate. Thus, we will use the simulated ion dynamic differences between the edge region of the 63.5° corner and the center region to analyze the different film properties between the edge region of the 60° corner and the center region for the *f*-plane in our experiment. Based on the highest hardness region (the edge region of the 60° corner) for the *f*-plane, herein, we select the ion flux density in the radial range of −12 mm to −30 mm (the edge region of 63.5° corner), as shown in Fig. 11, to evaluate the re-puttering effect of this edge region. Firstly, in order to get more data for evaluation, we use the method of Savitzky-Golay smooth with a 5-point windows (5-point SG) of signal processing on the ion flux density, as shown by the red balls in Fig. 11. Then by multiplying the smoothed ion flux with the sputtering yield at each point of this region, and averaging them lastly, we obtain the average re-sputtering rate with a value of ~2 and the average ion flux with a value of ~1.54. Although these values are estimated with errors, it seems consistent with experimental results that higher re-sputtering rate of the edge region results in the film thickness thinner than that in the center region, as shown in Fig. 8(a) and (b), combined with denser structure and smoother surface. In addition, the stronger ion flux bombardment in the edge region of the 63.5° corner may introduce heat to increase the adatom mobility, further condensing the structure, and bring in compressive stress [59], which may improve the film toughness and hardness, as shown in Figs. 5 and 6.

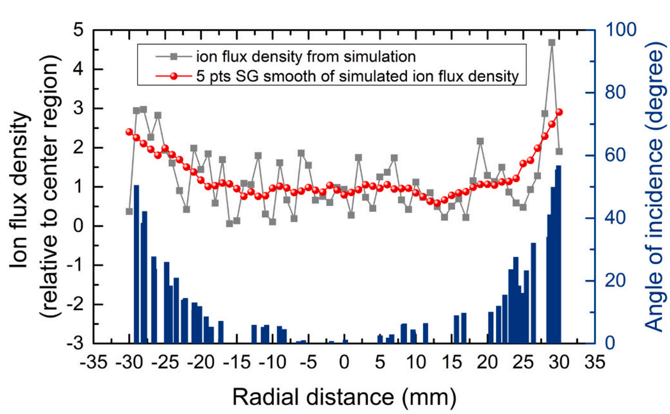

Fig. 11. The distribution of ion flux density (left, line chart), combined with angle of incidence of ions (right, bar chart), in front of *f*-plane (*z* = 60 mm) at *t* = 1.62 μs from PIC-MCC numerical simulation (at this moment, the plasma density is 1.7 × 10^{17} m^{-3} in front of the substrate).

Moreover, as the corner angle increase to116.5°, the contours of potential around its edge become much more expanded than that around 63.5° edges, as shown in Fig. 9(a). Then, for the *b*-plane, the focusing degree of the ion trajectories toward the edge of 116.5° corner reduced, and the angle of incidence of the ions become almost similar with the center region. The shadowing effect for the *b*-plane also plays a big role, where the ion flux is weakened down by its own geometry. As a result, the edge-related hardness region of 116.5° corner becomes very narrow for the *b*-plane.

One point should be cared that it's easy to be recognized that the transitions of the hardness between center region and edge region should be smooth on each plane. However, the abrupt changes of the hardness value always be here on these studied planes of our substrate. It may be due to the differences in their microstructure such as crystal orientation, refined grain size and so on, resulted from the different ion flux and re-sputtering, which need our further study in the forthcoming experiments.

4. Conclusion

In this work, the effects of geometric position on the film properties for a trapezoidal-prism substrate are studied in a homemade HiPIMS system with the example of TiAlSiN film, by experiments together with plasma dynamics simulation. The different ion flux, resulting from the shadowing effect, makes the film properties on the various planes dependent on their positions with respect to the target surface. As increasing the inclination angle of the planes with respect to the target surface, the hardness and toughness of film decreased significantly in order of on the *f*-plane, *p*-plane, and *b*-plane. For the same plane, it can be seen that the ion flux density is higher and the re-sputtering rate is larger in the edge regions of the corners than those in the center regions from the results of the PIC-MCC simulation and TRIM code. Then, the HiPIMS-deposited TiAlSiN films in the edge regions present the characteristics of thinner thickness, smoother surface, denser structure and a chemical composition with higher titanium and lower aluminum content. Consequently, the higher hardness of TiAlSiN films are expected in the edge regions, and their toughness is improved probably by the introduced compressive stress from stronger ion bombardment. This film with enhanced properties at the edges will be really advantageous to the cutting tools. In addition, if the corner angle becomes larger, the affected edge region will narrow, and the film properties tend to be uniform. However, there are always some abrupt changes of the hardness value between center region and edge region on these studied planes of our substrate. But presently, we cannot give the better explanation. Moreover, as the corner becomes sharper, as shown in simulated results, such as the corner angle ≤45°, the films in its edge regions may be delaminated or not deposited, which are of importance for guiding the industrial applications of high ion fraction plasma sources and the geometry design of the substrate for film deposition.

CRediT authorship contribution statement

Li Hua: Conceptualization, Simulation, Formal analysis, Methodology, Investigation, Data curation; Writing - original manuscript.

Luo Yang: Formal analysis, Data curation, Investigation, Review & editing.

Han Mingyue: Simulation, Data curation, Investigation, Review & editing.

Tang Ling: Formal analysis, Data Curation, Investigation.

Gu Jiabin: Data curation, Investigation, Review & editing.

Deng Dachen: Data curation, Investigation, Review & editing.

Huang Kai: Data curation, Investigation, Review & editing.

Liu Hongtao: Investigation, Review & editing.

Li Guodong: Methodology, Investigation, Validation, Review & editing.

Li Liuhe: Funding acquisition, Methodology, Supervision, Project administration.

Declaration of competing interest

The authors declare the following financial interests/personal relationships which may be considered as potential competing interests: Li Liuhe reports financial support was provided by National Science and Technology Major Project (2017-VII-0012-0108, 2017-VII-0003-0096).

Acknowledgements

The works were jointly supported by National Science and Technology Major Project (2017-VII-0012-0108, 2017-VII-0003-0096).

References

[1] M. Samuelsson, D. Lundin, J. Jensen, M.A. Raadu, J.T. Gudmundsson, U. Helmersson, On the film density using high power impulse magnetron sputtering, Surf. Coat. Technol. 205 (2010) 591–596, https://doi.org/10.1016/j.surfcoat.2010.07.041.

[2] J. Alami, P.O.Å. Persson, D. Music, J.T. Gudmundsson, J. Bohlmark, U. Helmersson, Ion-assisted physical vapor deposition for enhanced film properties on nonflat surfaces, J. Vac. Sci. Technol. A 23 (2005) 278–280, https://doi.org/10.1116/1.1861049.

[3] M. Lattemann, U. Helmersson, J.E. Greene, Fully dense, non-faceted 111-textured high power impulse magnetron sputtering TiN films grown in the absence of substrate heating and bias, Thin Solid Films 518 (2010) 5978–5980, https://doi.org/10.1016/j.tsf.2010.05.064.

[4] J.E. Sundgren, Structure and properties of TiN coatings, Thin Solid Films 128 (1985) 21–44, https://doi.org/10.1016/0040-6090(85)90333-5.

[5] W. Tillmann, M. Dildrop, Influence of si content on mechanical and tribological properties of TiAlSiN PVD coatings at elevated temperatures, Surf. Coat. Technol. 321 (2017) 448–454, https://doi.org/10.1016/j.surfcoat.2017.05.014.

[6] N. He, H. Li, L. Ji, X. Liu, H. Zhou, J. Chen, High temperature tribological properties of TiAlSiN coatings produced by hybrid PVD technology, Tribol. Int. 98 (2016) 133–143, https://doi.org/10.1016/j.triboint.2016.02.034.

[7] Y. Tanaka, N. Ichimiya, Y. Onishi, Y. Yamada, Structure and properties of A1-ti-si-N coatings prepared by the cathodic arc ion plating method for high speed cutting applications, Surf. Coat. Technol. 146 (2001) 215–221, https://doi.org/10.1016/S0257-8972(01)01391-3.

[8] A. Kumar, R. Bauri, A. Naskar, A.K. Chattopadhyay, Characterization of HiPIMS and DCMS deposited TiAlN coatings and machining performance evaluation in high speed dry machining of low and high carbon steel, Surf. Coat. Technol. 417 (2021), 127180, https://doi.org/10.1016/j.surfcoat.2021.127180.

[9] G. Li, J. Sun, Y. Xu, Y. Xu, J. Gu, L. Wang, K. Huang, K. Liu, L. Li, Microstructure, mechanical properties, and cutting performance of TiAlSiN multilayer coatings prepared by HiPIMS, Surf. Coat. Technol. 353 (2018) 274–281, https://doi.org/10.1016/j.surfcoat.2018.06.017.

[10] C.S. Kumar, S.K. Patel, Performance analysis and comparative assessment of nano-composite TiAlSiN/TiSiN/TiAlN coating in hard turning of AISI 52100 steel, Surf. Coat. Technol. 335 (2018) 265–279, https://doi.org/10.1016/j.surfcoat.2017.12.048.

[11] S. Koseki, K. Inoue, H. Usuki, Damage of physical vapor deposition coatings of cutting tools during alloy 718 turning, Precis. Eng. 44 (2016) 41–54, https://doi.org/10.1016/j.precisioneng.2015.09.012.

[12] H.C. Chen, K.H. Chen, Y.C. Xu, C.X. Pan, J.Y. Yi, Zhu, Microstructure, mechanical properties, and milling performance of arc-PVD AlTiN-Cu and AlTiN/AlTiN-Cu coatings, J. Cent. South Univ. Sci. Technol. Min. Metall. 3 (2018) 506–515, https://doi.org/10.1007/s11771-018-3755.

[13] K. Bobzin, N. Bagcivan, P. Immich, S. Bolz, J. Alami, R. Cremer, Advantages of nanocomposite coatings deposited by high power pulse magnetron sputtering technology, J. Mater. Process. Technol. 209 (2009) 165–170, https://doi.org/10.1016/j.jmatprotec.2008.01.035.

[14] Luca W. Reolon, Myriam H. Aguirre, Kenji Yamamoto, Qinfu Zhao, Igor Zhitomirsky, German Fox-Rabinovich, Stephen Clarence Veldhuis, A Comprehensive study of Al0.6Ti0.4N coatings deposited by cathodic arc and HiPIMS PVD methods in relation to their cutting performance during the machining of an inconel 718 alloy, Coatings 11 (2021) 723, https://doi.org/10.3390/coatings11060723.

[15] K. Bobzin, N. Bagcivan, P. Immich, S. Bolz, H.G. Fuß, R. Cremer, Properties of (Ti, Al, Si)N coatings for high demanding metal cutting applications deposited by HPPMS in an industrial coating unit, Plasma Process. Polym. 6 (2009) S124–S128, https://doi.org/10.1002/ppap.200930408.

[16] A.P. Kulkarni, G.G. Joshi, V.G. Sargade, Performance of PVD AlTiCrN coating during machining of austenitic stainless steel, Surf. Eng. 29 (2013) 402–407, https://doi.org/10.1179/1743294413Y.0000000130.

[17] M. Balzer, M. Fenker, Three-dimensional thickness and property distribution of TiC films deposited by DC magnetron sputtering and HIPIMS, Surf. Coat. Technol. 250 (2014) 37–43, https://doi.org/10.1016/j.surfcoat.2014.02.011.

[18] V. Kouznetsov, K. MacÁk, J.M. Schneider, U. Helmersson, I. Petrov, A novel pulsed magnetron sputter technique utilizing very high target power densities, Surf. Coat. Technol. 122 (1999) 290–293, https://doi.org/10.1016/S0257-8972(99)00292-3.

[19] D. Mozgrin, I. Fetisov, G. Khodachenko, High-current low-pressure quasi-stationary discharge in a magnetic field: experimental research, Plasma Phys. Rep. 21 (1995) 400–409.

[20] J.T. Gudmundsson, The high power impulse magnetron sputtering discharge as an ionized physical vapor deposition tool, Vacuum 84 (2010) 1360–1364, https://doi.org/10.1016/j.vacuum.2009.12.022.

[21] A.P. Ehiasarian, R. New, W.D. Münz, L. Hultman, U. Helmersson, V. Kouznetsov, Influence of high power densities on the composition of pulsed magnetron plasmas, Vacuum 65 (2002) 147–154, https://doi.org/10.1016/S0042-207X(01)00475-4.

[22] J.T. Gudmundsson, J. Alami, U. Helmersson, Evolution of the electron energy distribution and plasma parameters in a pulsed magnetron discharge, Appl. Phys. Lett. 78 (2001) 3427–3429, https://doi.org/10.1063/1.1376150.

[23] J. Bohlmark, J.T. Gudmundsson, J. Alami, M. Latteman, U. Helmersson, Spatial electron density distribution in a high-power pulsed magnetron discharge, IEEE Trans. Plasma Sci. 33 (2005) 346–347, https://doi.org/10.1109/tps.2005.845022.

[24] Y. Xu, G. Li, G. Li, F. Gao, Y. Xia, Effect of bias voltage on the growth of super-hard (AlCrTiVZr)N high-entropy alloy nitride films synthesized by high power impulse magnetron sputtering, Appl. Surf. Sci. 564 (2021), 150417, https://doi.org/10.1016/j.apsusc.2021.150417.

[25] T. Lin, L. Wang, X. Wang, Y. Zhang, Y. Yu, Influence of bias voltage on microstructure and phase transition properties of VO2 thin film synthesized by HiPIMS, Surf. Coat. Technol. 305 (2016) 110–115, https://doi.org/10.1016/j.surfcoat.2016.08.020.

[26] K. Bobzin, N. Bagcivan, P. Immich, S. Bolz, R. Cremer, T. Leyendecker, Mechanical properties and oxidation behaviour of (Al, Cr)N and (Al, cr, Si)N coatings for cutting tools deposited by HPPMS, Thin Solid Films 517 (2008) 1251–1256, https://doi.org/10.1016/J.TSF.2008.06.050.

[27] N. Bagcivan, K. Bobzin, S. Theiß, Comparison of (Cr0.75Al0.25)N coatings deposited by conventional and high power pulsed magnetron sputtering, Contrib. Plasma Phys. 52 (2012) 601–606, https://doi.org/10.1002/ctpp.201210056.

[28] P.A. Watterson, Child-langmuir sheath structure around wedge-shaped cathodes, J. Phys. D. Appl. Phys. 22 (1989) 1300–1307, https://doi.org/10.1088/0022-3727/22/9/009.

[29] I.J. Donnelly, P.A. Watterson, Ion-matrix sheath structure around cathodes of complex shape, J. Phys. D. Appl. Phys. 22 (1989) 90–93, https://doi.org/10.1088/0022-3727/22/1/012.

[30] M. Čada, P. Adámek, V. Straňák, Š. Kment, J. Olejníček, Z. Hubička, R. Hippler, Angle-resolved investigation of ion dynamics in high power impulse magnetron sputtering deposition system, Thin Solid Films 549 (2013) 177–183, https://doi.org/10.1016/j.tsf.2013.06.061.

[31] R. Hippler, Z. Hubicka, M. Cada, P. Ksirova, H. Wulff, C.A. Helm, V. Stranak, Angular dependence of plasma parameters and film properties during high power impulse magnetron sputtering for deposition of ti and TiO2 layers, J. Appl. Phys. 121 (2017), https://doi.org/10.1063/1.4977823.

[32] Q. Ma, L. Li, Y. Xu, X. Ma, Y. Xu, H. Liu, Effect of ti content on the microstructure and mechanical properties of TiAlSiN nanocomposite coatings, Int. J. Refract. Met. Hard Mater. 59 (2016) 114–120, https://doi.org/10.1016/j.ijrmhm.2016.06.005.

[33] Q. Ma, L. Li, Y. Xu, J. Gu, L. Wang, Y. Xu, Effect of bias voltage on TiAlSiN nanocomposite coatings deposited by HiPIMS, Appl. Surf. Sci. 392 (2017) 826–833, https://doi.org/10.1016/j.apsusc.2016.09.028.

[34] O. Buneman, in: R. Hockney, J.W. Eastwood (Eds.), Computer-Simulation Using Particles, 1983, https://doi.org/10.1137/1025102.

[35] M.A. Liberman, J.L. Allan, Principles of Plasma Discharges and Materials Processing, Wiley, New York, 1994.

[36] M. Han, Y. Luo, H. Li, Y. Xu, S. Luo, H. Xu, C. Xu, L. Li, Effects of the dynamic cathode sheath on electron transport at the initial period of HiPIMS pulse studied by langmuir probe measurements and 2D PIC-MCC simulation, Surf. Coat. Technol. 403 (2020), https://doi.org/10.1016/j.surfcoat.2020.126371.

[37] A. Revel, T. Minea, C. Costin, 2D PIC-MCC simulations of magnetron plasma in HiPIMS regime with external circuit, Plasma Sources Sci. Technol. 27 (2018), https://doi.org/10.1088/1361-6595/aadebe.

[38] D.T.K. Kwok, S. Wu, X. Liu, R.K.Y. Fu, P.K. Chu, Investigation of plasma immersion ion implantation of nickel-titanium rod by multiple-grid particle-in-cell simulation, J. Appl. Phys. 103 (2008), https://doi.org/10.1063/1061.2890157.

[39] M. Han, Y. Luo, H. Li, L. Li, Y. Xu, S. Luo, P. Zhang, H. Xu, C. Xu, Auxiliary capacitor to enhance oscillation in circuit and reduce current onset delay in

HiPIMS discharge: theory, experiment and simulation, Surf. Coat. Technol. 405 (2021), https://doi.org/10.1016/j.surfcoat.2020.126518.
[40] M. Han, Y. Luo, L. Tang, J. Gu, H. Li, Y. Xu, S. Luo, L. Li, Plasma flux and energy enhancement in BP-HiPIMS discharge via auxiliary anode and solenoidal coil, Plasma Sources Sci. Technol. 30 (2021), https://doi.org/10.1088/1361-6595/ac1082c1088c.
[41] Y. Xu, L. Li, S. Luo, Q. Lu, J. Gu, N. Lei, C. Huo, Self-enhanced plasma discharge effect in the deposition of diamond-like carbon films on the inner surface of slender tube, Appl. Surf. Sci. 393 (2017) 467–473, https://doi.org/10.1016/j.apsusc.2016.10.049.
[42] L. Li, J. Li, D.T.K. Kwok, Z. Wang, P.K. Chu, Plasma sheath physics and dose uniformity in enhanced glow discharge plasma immersion ion implantation and deposition, J. Appl. Phys. 106 (2009), https://doi.org/10.1063/1.3160309.
[43] A. Kramida, R. Yu, Reader J (NIST ASD Team), NIST atomic spectra database (version 5.8), National Institute of Standards and Technology, Gaithersburg MD, 2020. https://physics.nist.gov/asd.
[44] J. Bretagne, G. Callede, M. Legentil, V. Puech, Relativistic electron-beam-produced plasmas. I. Collision cross sections and loss function in argon, J. Phys. D. Appl. Phys. 19 (1986) 761–777, https://doi.org/10.1088/0022-3727/19/5/010.
[45] V. Vahedi, M. Surendra, A Monte Carlo collision model for the particle-in-cell method: applications to argon and oxygen discharges, Comput. Phys. Commun. 87 (1995) 179–198, https://doi.org/10.1016/0010-4655(94)00171-W.
[46] M. Stoiber, C. Mitterer, T. Schoeberl, E. Badisch, G. Fontalvo, R. Kullmer, Nanocomposite coatings within the system Ti–B–N deposited by plasma assisted chemical vapor deposition, J. Vac. Sci. Technol., B: Microelectron. Nanometer Struct.–Process., Meas., Phenom. 21 (2003) 1084, https://doi.org/10.1116/1.1570846.
[47] Y.W. Bao, C.C. Liu, J.L. Huang, Effects of residual stresses on strength and toughness of particle-reinforced TiN/Si3N4 composite: theoretical investigation and FEM simulation, Mater. Sci. Eng. A 434 (2006) 250–258, https://doi.org/10.1016/j.msea.2006.06.136.
[48] J. Pelleg, L.Z. Zevin, S. Lungo, N. Croitoru, Reactive-sputter-deposited TiN films on glass substrates, Thin Solid Films 197 (1991) 117–128, https://doi.org/10.1016/0040-6090(91)90225-M.
[49] W. Stowell, Throwing power and shadowing effect in planar magnetron sputtering process, J. Vac. Sci. Technol. A 3 (1985), https://doi.org/10.1116/1.572996.
[50] K.M. Calamba, I.C. Schramm, M.P.Johansson Jõesaar, J. Ghanbaja, J.F. Pierson, F. Mücklich, M. Odén, Enhanced thermal stability and mechanical properties of nitrogen deficient titanium aluminum nitride (Ti0.54Al0.46Ny) thin films by tuning the applied negative bias voltage, J. Appl. Phys. 122 (1–10) (2017), https://doi.org/10.1063/1.4986350, 065301.
[51] R. Messier, A.P. Giri, R.A. Roy, Revised structure zone model for thin film physical structure, J. Vac. Sci. Technol. A 2 (1984) 500–503, https://doi.org/10.1116/1.572604.
[52] G. Li, L. Li, M. Han, S. Luo, J. Jin, L. Wang, J. Gu, H. Miao, The performance of TiAlSiN coated cemented carbide tools enhanced by inserting ti interlayers, Metals (Basel) 9 (2019) 918, https://doi.org/10.3390/met9090918.
[53] A.J. Perry, On the existence of point defects in physical vapor deposited films of TiN, ZrN, and HfN, J. Vac. Sci. Technol. A 6 (1988) 2140–2148, https://doi.org/10.1116/1.575205.
[54] H.S. Park, D.H. Jung, H.D. Na, J.H. Joo, J.J. Lee, The properties of (Ti, Al)N coatings deposited by inductively coupled plasma assisted d.c. magnetron sputtering, Surf. Coat. Technol. 142–144 (2001) 999–1004, https://doi.org/10.1016/S0257-8972(01)01217-8.
[55] J.M. Molarius, A.S. Korhonen, E. Harju, R. Lappalainen, Comparison of cutting performance of ion-plated NbN, ZrN, TiN and (Ti, Al)N coatings, Surf. Coat. Technol. 33 (1987) 117–132, https://doi.org/10.1016/0257-8972(87)90182-4.
[56] H. Oettel, R. Wiedemann, S. Preißler, Residual stresses in nitride hard coatings prepared by magnetron sputtering and arc evaporation, Surf. Coat. Technol. 74–75 (1995) 273–278, https://doi.org/10.1016/0257-8972(95)08235-2.
[57] E.B. Macak, W.D. Münz, J.M. Rodenburg, Electron microscopy studies of hard coatings deposited on sharp edges by combined cathodic arc/unbalanced magnetron PVD, Surf. Coat. Technol. 151–152 (2002) 349–354, https://doi.org/10.1016/S0257-8972(01)01650-4.
[58] E.B. Macak, W.D. Münz, J.M. Rodenburg, Plasma-surface interaction at sharp edges and corners during ion-assisted physical vapor deposition. Part I: edge-related effects and their influence on coating morphology and composition, J. Appl. Phys. 94 (2003) 2829–2836, https://doi.org/10.1063/1.1597755.
[59] James F. Ziegler. http://www.srim.org/.